Nuclear Magnetic Resonance in Inhomogeneous Magnetic Fields

F. Bălibanu,[1,†] Kidist Hailu, R. Eymael, D. E. Demco, and B. Blümich[2]

Institut für Technische Chemie und Makromolekulare Chemie, Rheinisch-Westfälische Technische Hochschule, Worringerweg 1, D-52056 Aachen, Germany

The response of the spin system has been investigated by numerical simulations in the case of a nuclear magnetic resonance (NMR) experiment performed in inhomogeneous static and radiofrequency fields. The particular case of the NMR-MOUSE was considered. The static field and the component of the radiofrequency field perpendicular to the static field were evaluated as well as the spatial distribution of the maximum NMR signal detected by the surface coil. The NMR response to various pulse sequences was evaluated numerically for the case of an ensemble of isolated spins $\frac{1}{2}$. The behavior of the echo train in Carr–Purcell-like pulse sequences used for measurements of transverse relaxation and self-diffusion was simulated and compared with the experiment. The echo train is shown to behave qualitatively differently depending on the particular phase schemes used in these pulse sequences. Different echo trains are obtained, because of the different superposition of Hahn and stimulated echoes forming mixed echoes as a result of the spatial distribution of pulse flip angles. The superposition of Hahn and stimulated echoes originating from different spatial regions leads to distortions of the mixed echoes in intensity, shape, and phase. The volume selection produced by Carr–Purcell-like pulse sequences is also investigated for the NMR-MOUSE. The developed numerical simulation procedure is useful for understanding a variety of experiments performed with the NMR-MOUSE and for improving its performance.   © 2000 Academic Press

Key Words: NMR-MOUSE; inhomogeneous fields; Carr–Purcell pulse sequence; mixed echo; virtual echo; selective volume.

INTRODUCTION

High-resolution nuclear magnetic resonance (NMR) of liquid and solid samples uses excitation and detection of NMR signals with homogenous radiofrequency and static magnetic fields (*1, 2*). This ensures well-defined flip angles which are important for predicting the spin evolution and reveals the internuclear couplings as a source of structural and dynamic information (*1–5*). Nevertheless, controlled inhomogenous static and/or radiofrequency fields have been used in NMR spectroscopy for enhanced coherences selection (*6–8*),

in NMR imaging, and in volume localized spectroscopy (*4, 9–11*).

Magnetic field gradients are an asset for obtaining spatial resolution, and their continuous presence allows in principle for the determination of transverse and longitudinal relaxation and they enable measurements of translational diffusion. Thus NMR devices for spatially resolved material characterization can be constructed with inhomogeneous magnetic fields, without the need for the superconducting magnet, the most expensive component in commercial imaging equipment. Based on these considerations, the NMR-MOUSE (mobile universal surface explorer) has been developed (*12–16*). It has been shown that relaxation measurements by the NMR-MOUSE are useful in nondestructive, *in situ* characterization of polymers (*12–15*).

In contrast to conventional NMR where the probe supplies only the radiofrequency magnetic field $\mathbf{B}_1$, the NMR MOUSE probe consists of two permanent magnets with anti-parallel magnetization producing the $\mathbf{B}_0$ field. For radiofrequency irradiation, a surface coil is mounted in between the magnets. A similar approach can be found in Ref. (*17*). The advantage of this concept is that limitations of the sample size no longer exist. However, the sensitive volume is restricted to regions near the surface of the object under examination. It depends on the configuration of the $\mathbf{B}_0$ and $\mathbf{B}_1$ fields and is therefore determined by the geometry of the permanent magnets and of the radiofrequency coil.

The given inhomogeneities of $\mathbf{B}_0$ and $\mathbf{B}_1$ require reexamination of the spin system response to the well-known pulse sequences. The aim of this work is to gain an improved understanding of the origin of the measured NMR signal as well as its spatial distribution, and the shape and intensity of the spin echoes. In particular the behavior of the echo train is investigated in the Carr–Purcell-like pulse sequences (*18–22*) used for measurements of transverse relaxation and self-diffusion. The echo train is shown to behave qualitatively differently depending on the phase schemes used. Variation in the echo trains are shown to result from different superposition of Hahn and stimulated echoes forming *mixed* echoes (*23*) as a result of the spatial distribution of pulse flip angles. The volume selection of Hahn and stimulated echoes which is elective in mixed echoes as well as that in Carr–Purcell-like pulse sequences is also investigated. The analysis is performed

---

[1] On leave from the Institute for Isotopic and Molecular Technology, P.O.B. 700, RO 3400 Cluj-Napoca, Romania.

[2] To whom correspondence should be addressed.

† Deceased.

by numerical simulation of the spin system response in the case of noninteracting spins.

NUMERICAL SIMULATION OF THE NMR SIGNAL

For simulation of the signal of the NMR-MOUSE, the sample is divided into volume elements, hereafter called *voxels*. The simulation comprised four steps: (i) computation of the static magnetic field $\mathbf{B}_0$ in each of the volume elements; (ii) computation of the radiofrequency field $\mathbf{B}_{RF}$ in the same points; (iii) calculation of the evolution of the nuclear spins under the influence of the radiofrequency sequence in each voxel; (iv) calculation of the electric signal induced in the coil by the nuclear spins.

The Static Magnetic Field $\mathbf{B}_0(\mathbf{r})$

The magnetic field generated by the permanent magnets has been computed as a Coulombian field by using the surface charge approximation (*24*). By considering the magnetic charges distributed on the surface of the permanent magnets that face the sample $\mathbf{B}_0$ at a point $\mathbf{r}$ is computed according to

$$\mathbf{B}_0(\mathbf{r}) = k\left(\int_{S_1} \frac{\mathbf{r} - \mathbf{r}_1}{\|\mathbf{r} - \mathbf{r}_1\|^3}\, ds - \int_{S_2} \frac{\mathbf{r} - \mathbf{r}_2}{\|\mathbf{r} - \mathbf{r}_2\|^3}\, ds \right), \quad [1]$$

where S_1 and S_2 are North and South pole surfaces, and $\mathbf{r}_1$ and $\mathbf{r}_2$ denote the positions of the surface elements. All vectors describing positions refer to the same arbitrarily selected reference frame. The symbol $\|(\dots)\|$ denotes the vector modulus. The mesh size of the integration grid was selected considering the minimum distance from the pole surfaces where $\mathbf{B}_0$ is computed. The typical value is 0.2 mm. The value of constant k was determined by fitting the computed values to the measured ones for the particular device considered.

The geometry of the $\mathbf{B}_0(\mathbf{r})$ field can be represented by isosurfaces, solutions of the implicit equation $\mathbf{B}_0(\mathbf{r}) = $ const. Figure 1 displays the isosurfaces that cross the axis of the radiofrequency coil at 5 and 3 mm (cf. Figs. 1a and 1b, respectively).

The evaluation of the magnetic flux density described above has some limitations: The magnetic charges were considered to be distributed uniformly on the two surfaces, and no interaction between the elementary magnetic moments was taken into account. As a consequence deviations from the field are larger close to the NMR-MOUSE surface, i.e., in the sensitive volume of the device. Nevertheless, this approximation of $\mathbf{B}_0(\mathbf{r})$ produces satisfactory results (see below).

The Radiofrequency Field

The field produced by the transmitter coil can be calculated using the Biot-Savart law (*25*), i.e.,
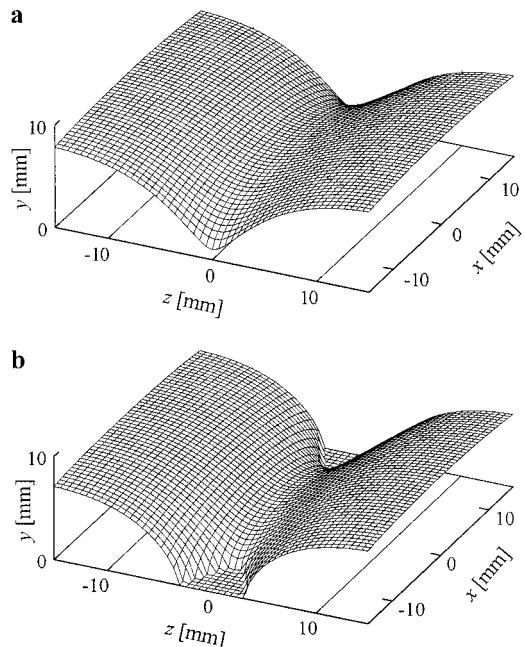

FIG. 1. Isosurfaces, solutions of $\mathbf{B}_0(\mathbf{r})$ centered at $\mathbf{r} = (0, 5\text{ mm}, 0)$ (a), and $\mathbf{r} = (0, 3\text{ mm}, 0)$ (b).

$$\mathbf{B}_{RF}(\mathbf{r}) = \frac{\mu_0 I}{4\pi} \oint \frac{(\mathbf{r}_1 - \mathbf{r}) \times d\mathbf{r}_1}{\|\mathbf{r}_1 - \mathbf{r}\|^3} = I\mathbf{b}_{RF}, \quad [2]$$

where I is the current in the coil and μ_0 is the vacuum permeability. In Eq. [2], $\mathbf{r}_1$ is the position of the coil element of length $d\mathbf{r}_1$. The magnetic flux density per unit current $\mathbf{b}_{RF}$ was computed by numerical integration along the windings of the coil.

In an NMR experiment it is customary to replace $\mathbf{b}_{RF}$ by $2\mathbf{b}_1$, and, in the case of strong inhomogeneous fields, one needs to consider that only the component of $\mathbf{B}_1$ orthogonal to $\mathbf{B}_0$ (henceforth denoted $\mathbf{B}_{1n}$), induces quantum transitions because the parallel component commutes with the Zeeman Hamiltonian. For this reason the values of $\mathbf{b}_{1n}$ were computed at the same points where $\mathbf{B}_0$ was computed.

The strength of the radiofrequency (RF) field $\mathbf{b}_{1n}$ relevant for the NMR experiment was evaluated with some approximations: The presence of objects near the RF coil was neglected. This concerns in particular the permanent magnets that greatly distort the RF field. The finite diameter of the coil wire has also been neglected. For computational commodity the coil was approximated by a set of circles.

It can be seen below that despite these approximations in the calculation of $\mathbf{B}_0$ and $\mathbf{B}_1$ the quantitative computations for the NMR-MOUSE remain fairly accurate.

The Evolution of the Spin System

A system of isolated spins $\frac{1}{2}$ is considered which interacts with two magnetic fields $\mathbf{B}_0(\mathbf{r})$ and $\mathbf{B}_1(\mathbf{r},\ t)$. In the high-

temperature approximation (*1, 2*) for such a system the density operator of each voxel can be written as

$$\rho(t) \propto E + \frac{\gamma \hbar B_0}{k_B T} [C_1(t)\mathbf{I}_x + C_2(t)\mathbf{I}_y + C_3(t)\mathbf{I}_z]. \quad [3]$$

In this equation the explicit dependence on **r** has been dropped. E is the unity operator, $\mathbf{I}$ ($\mathbf{I}_x$, $\mathbf{I}_y$, $\mathbf{I}_z$) is the total spin operator, γ is the magnetogyric factor, k_B is the Boltzmann constant, and T is the absolute temperature. The Liouville space coordinates of the density operator are given by the coefficients $C_i(t)$ where $i = 1, 2, 3$. As the unity operator E commutes with all other operators and if all we intend to calculate is the average values of the traceless spin operators, the density operator can be reduced to

$$\rho(t) \propto [C_1(t)\mathbf{I}_x + C_2(t)\mathbf{I}_y + C_3(t)\mathbf{I}_z]. \quad [4]$$

Coefficients C_1, C_2, and C_3 are changing in time under the influence of spin interactions, and our calculations are similar to those described by other authors (*26*).

In the absence of the RF field, the components of the density matrix in a reference frame rotating with ω around the local $-z$ direction evolve according to

$$\mathbf{I}_x \rightarrow \mathbf{I}_x \cos(\omega_0 - \omega)t - \mathbf{I}_y \sin(\omega_0 - \omega)t,$$
$$\mathbf{I}_y \rightarrow \mathbf{I}_y \cos(\omega_0 - \omega)t + \mathbf{I}_x \sin(\omega_0 - \omega)t,$$
$$\mathbf{I}_z \rightarrow \mathbf{I}_z. \quad [5]$$

The local z direction is aligned with the local static magnetic field $\mathbf{B}_0$ and the local Larmor frequency is given by $\omega_0 = \gamma B_0$. Transverse and longitudinal relaxation can be introduced phenomenologically in the above equations.

After the action of a hard pulse the evolution of the density matrix can be calculated from the following transformations:

$$\mathbf{I}_x \rightarrow \mathbf{I}_x(\cos \alpha \cos^2\theta \cos^2\varphi + \cos \alpha \sin^2\varphi + \sin^2\theta \sin^2\varphi)$$
$$+ \mathbf{I}_y(\cos \alpha \cos^2\theta \sin \varphi \cos \varphi - \cos \alpha \sin \varphi \cos \varphi$$
$$+ \sin \alpha \cos \theta + \sin^2\theta \sin \varphi \cos \varphi)$$
$$+ \mathbf{I}_z(-\cos \alpha \sin \theta \cos \theta \sin \varphi - \sin \alpha \sin \theta \sin \varphi$$
$$+ \sin \theta \cos \theta \cos \varphi),$$
$$\mathbf{I}_y \rightarrow \mathbf{I}_x(-\sin \alpha \cos \theta - \cos \alpha \sin^2\theta \sin \varphi \cos \varphi$$
$$+ \sin^2\theta \sin \varphi \cos \varphi)$$
$$+ \mathbf{I}_y(\cos \alpha \cos^2\theta \sin^2\varphi + \cos \alpha \cos^2\varphi$$
$$+ \sin^2\theta \sin^2\varphi)$$
$$+ \mathbf{I}_z(-\cos \alpha \sin \theta \cos \theta \sin \varphi$$
$$+ \sin \alpha \sin \theta \sin \varphi + \sin \theta \cos \theta \cos \varphi),$$

$$\mathbf{I}_z \rightarrow \mathbf{I}_x(-\cos \alpha \sin \theta \cos \theta \cos \varphi + \sin \alpha \sin \theta \sin \varphi$$
$$+ \sin \theta \cos \theta \cos \varphi)$$
$$+ \mathbf{I}_y(-\cos \alpha \sin \theta \cos \theta \sin \varphi + \sin \alpha \sin \theta \cos \varphi$$
$$+ \sin \theta \cos \theta \sin \varphi)$$
$$+ \mathbf{I}_z(\cos \alpha \sin^2\theta + \cos^2\theta). \quad [6]$$

In the above equations the local flip angle is $\alpha = \sqrt{(\omega_0 - \omega)^2 + \omega_1^2} \cdot t_w \equiv \omega_{eff} t_w$, where ω_1 is the strength of the RF pulse and ω is the irradiation frequency. t_w is the duration of the RF pulse and φ is the phase of the RF field $B_{RF}(t) = 2B_{1n}\cos(\omega t + \varphi)$. The azimuthal angle θ is the angle between the effective field and $\mathbf{B}_0$. All of the above quantities, except for ω, φ, and t_w, depend on the voxel position. Relaxation during the pulses was neglected.

The NMR Signal

The signal induced by the magnetic moment **m** of a volume element of the sample at position **r** in the receiver coil is given by

$$e = -\frac{\partial \Phi_m}{\partial t} = -\frac{\partial}{\partial t} \int_S (\mathbf{B}_m \cdot \mathbf{n})dS, \quad [7]$$

where Φ_m is the magnetic flux trough the coil created by the magnetic moment **m** of the voxel, $\mathbf{B}_m$ is the corresponding magnetic flux density, and **n** is the unit vector orthogonal to the surface element dS of the coil. Using the Stokes theorem (*25*), the surface integral can be replaced by the contour integral of the vector potential $\mathbf{A}_m$,

$$\Phi_m = \int_S (\mathbf{B}_m \cdot \mathbf{n})dS = \int_S (\nabla \times \mathbf{A}_m) \cdot \mathbf{n}dS = \oint_L \mathbf{A}_m \cdot d\mathbf{r}. \quad [8]$$

The vector potential generated by the magnetic moment **m** at the position $\mathbf{r}_1$ of the coil can be written (*27*) in the notation of Eq. [2] as

$$\mathbf{A}_\mu = \frac{\mu_0}{4\pi} \frac{\mathbf{m} \times (\mathbf{r}_1 - \mathbf{r})}{\|\mathbf{r}_1 - \mathbf{r}\|^3}. \quad [9]$$

If the transmitter and the receiver coils are the same, Eq. [8] becomes by, using Eq. [2], (*28*),

$$\Phi_m = \frac{\mu_0}{4\pi} \oint_L \frac{[\mathbf{m} \times (\mathbf{r}_1 - \mathbf{r})] \cdot d\mathbf{r}}{\|\mathbf{r}_1 - \mathbf{r}\|^3}$$

$$= \frac{\mu_0}{4\pi} \mathbf{m} \cdot \oint_L \frac{(\mathbf{r}_1 - \mathbf{r}) \times d\mathbf{r}}{\|\mathbf{r}_1 - \mathbf{r}\|^3}$$

$$= \mathbf{m} \cdot \mathbf{b}_{RF}. \qquad [10]$$

For further calculation a local coordinate system for a voxel is defined with the unit vectors $\mathbf{u}$, $\mathbf{v}$, and $\mathbf{w}$, where $\mathbf{w}$ is the local direction of the static magnetic field $\mathbf{B}_0$, $\mathbf{u}$ is the direction of the normal component $\mathbf{B}_{1n}$ of the radiofrequency field, and $\mathbf{v} = \mathbf{w} \times \mathbf{u}$ is orthogonal to both $\mathbf{B}_0$ and $\mathbf{B}_{1n}$.

Following a pulse, the local magnetization $\mathbf{m}$ of a volume element ΔV precesses around the local $\mathbf{w}$ axis with the Larmor frequency $\omega_0 = \gamma B_0$, which is assumed to be proportional to the local static magnetic field, i.e., $\mathbf{m} = \chi \mathbf{B}_0 \Delta V$, where χ is the nuclear magnetic susceptibility. This last quantity is proportional with γ^2 (2). In the absence of relaxation, the precessing magnetization can be written as

$$\mathbf{m}(t) = \chi B_0 \Delta V\{[\mathbf{u} \cos(\omega_0 t + \varphi)$$
$$- \mathbf{v} \sin(\omega_0 t + \varphi)]\sin \theta + \mathbf{w} \cos \theta\}, \quad [11]$$

where both φ and θ depend on the pulse sequence (length, timing, intensity, frequency, and phase of the pulses) and the local fields at the voxel position ($\mathbf{B}_0$ and $\mathbf{b}_{1n}$). The time evolving magnetization can be calculated from the C_i coefficients of Eq. [4], as

$$\mathbf{m}(t) = \gamma \hbar \, \text{Tr}\{\mathbf{I} \cdot \rho(t)\}. \qquad [12]$$

Using Eqs. [10], [7], and [11], the electric signal induced in the coil by an arbitrary voxel is obtained,

$$e = \chi \Delta V \gamma \mathbf{B}_0^2 b_{RF} \cos(\mathbf{b}_{RF}, \mathbf{u})\sin(\omega_0 t + \varphi)\sin(\theta)$$
$$= 2\chi \Delta V \gamma \mathbf{B}_0^2 b_{1n}[C_1(0)\sin(\omega_0 t + \Phi)$$
$$+ C_2(0)\cos(\omega_0 t + \Phi)], \qquad [13]$$

where Φ is a phase factor related to the transformation from the local rotating frame to the local laboratory frame and $\cos(\mathbf{b}_{RF}, \mathbf{u})$ is the cosine angle between the magnetic flux density per unit current $\mathbf{b}_{RF}$ and $\mathbf{u}$ vector.

At this stage new quantities called *signal densities* are introduced. They are defined as

$$S_{max}(\mathbf{r}) = 2\chi \gamma B_0^2 b_{1n},$$
$$S_x(\mathbf{r}, t) = 2\chi \gamma B_0^2 b_{1n} C_1(t),$$
$$S_y(\mathbf{r}, t) = 2\chi \gamma B_0^2 b_{1n} C_2(t). \qquad [14]$$

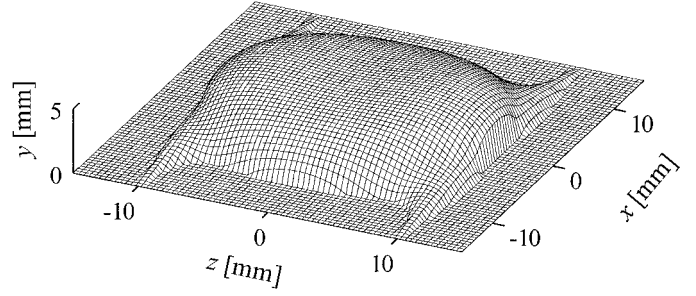**FIG. 2.** Isosurface of the response for $S_{max} = \frac{1}{2} S_{max}(0, 0, 0)$.

S_{max} is the *spatial responsivity* of the NMR device, while S_x and S_y are actual signals generated in a unit volume that can be phase detected at time t. The quantity S_{max} is the key to evaluating the sensitive volume of the NMR-MOUSE. Figure 2 shows an isosurface of the response that separates points with $S_{max} > 0.5\, S_0$ from points with $S_{max} < 0.5\, S_0$, where S_0 is the responsivity of the NMR-MOUSE at the surface in the center of the RF coil.

Based on this consideration the signal produced by any sequence of rectangular pulses can be computed by starting with an initial density matrix defined by the I_z component in the rotating frame, calculating its evolution by using Eqs. [5] and [10], and then computing the signals by Eq. [14]. The overall signal S_α, with $\alpha = x, y$, can be computed by integrating the signal density $S_\alpha(\mathbf{r})$ (cf. Eq.[14]) over the volume of the sample. If one wants to evaluate the effects of a receiver filter described by the function $f(\omega)$ it is very convenient to introduce the filter in our calculations at this step. The resulting signal at any time t is given by

$$s_{x,y}(t) = 2\chi \gamma \int_V B_0^2(\mathbf{r}) b_{1n}(\mathbf{r}) C_{1,2}(\mathbf{r}, t) f(\gamma B_0(\mathbf{r})) dV. \quad [15]$$

The quantities $C_{1,2}$ depend on $\mathbf{r}$ through the local fields $\mathbf{B}_0$ and $\mathbf{B}_{1n}$. For a heterogeneous sample the magnetic susceptibility is space dependent, i.e., $\chi(\mathbf{r})$, and has to remain inside the kernel of the integral.

The frequency distribution of a signal can be calculated as

$$S_\alpha(\omega) = \int_V S_\alpha(\mathbf{r})\delta(\omega - \gamma B_0(\mathbf{r})) dV, \qquad [16]$$

where δ is Dirac's delta function and $S_\alpha(\mathbf{r})$ is given by Eq. [14]. For the purpose of simulation Eqs. [15] and [16] have to be quantified and a suitable window function has to be used to approximate the Dirac function. In a similar manner one can obtain the distribution of the signal versus B_{1n}. The frequency distribution of the spatial responsivity, $dS_{max}/d\omega$, can be inter-
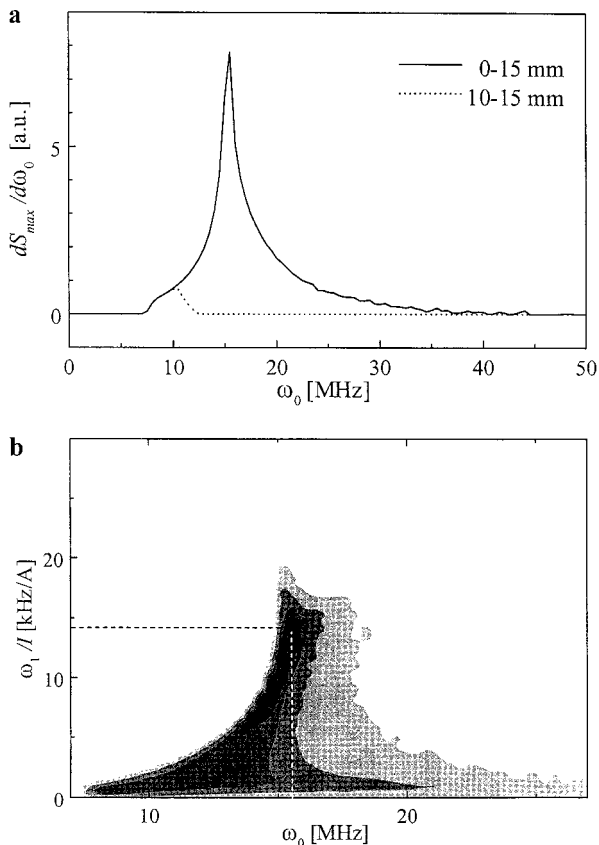
a

b

FIG. 3. (a) The frequency distribution of the maximum response signal for the NMR MOUSE. The width of this spectrum shows that any applied pulse is a selective one. (b) Two-dimensional distribution of the maximum response signal, versus $\omega_0 = \gamma B_0$ and $\omega_1/I = \gamma b_{1n}$. The maximum of the 2D distribution is observed at $\mathbf{r}(0, 0, 0)$. There $\omega_0 = 15.5$ MHz, and $\omega_1/I = 14.2$ kHz/A (marked at the intersection of the dotted lines).

preted as the *frequency responsivity spectrum* of the NMR-MOUSE (cf. Fig. 3a).

Even more informative about NMR experiments in inhomogeneous fields is the distribution of the spatial responsivity versus B_0 and B_{1n}. This is presented in Fig. 3b. The maximum of this function is at the origin $\mathbf{r} = (0, 0, 0)$, which is on the surface of the NMR-MOUSE in the center of the RF coil. This point is the most sensitive one because it is closest both to the three-dimensional saddle point of $\mathbf{B}_0$ and to the three-dimensional saddle point of $\mathbf{B}_{1n}$. This also means that the excited volume is largest when a pulse sequence is tuned for the point $\mathbf{r} = (0, 0, 0)$. The *ridge* going from that points toward $(\omega_0, \omega_1) = (0, 0)$ corresponds to the symmetry axis of the RF coil, going away from the surface of the NMR-MOUSE.

SPIN ECHOES IN INHOMOGENEOUS FIELDS

Numerical Simulation Test

In order to check the accuracy of this approach, an echo train generated by a Carr–Purcell XY16 pulse sequence (*21, 22, 29*)

has been simulated by considering the effects of various 90° and 180° pulses. In inhomogeneous fields the definition of 90° and 180° pulses is not trivial. While the phase and the length of the pulses are the same for all regions of the sample, their flip angle and resonance offset are strongly distributed in the sample volume. The 90° pulse cannot be selected as the one that maximizes the amplitude of the FID, because essentially FID is not longer than the pulse that excites it. Also, Fig. 3a underlines that there is no realistic pulse which can excite the entire spectrum, but only its own bandwith. Thus, for extended objects, the FID is unobservable in most cases. When trying to maximize the amplitude of an echo one is searching for a maximum in a two-dimensional space, because both the intensity (power) and the length of the pulses can be varied, and the maximum is never reached, except in the limit $t_w \rightarrow 0$ and $I \rightarrow \infty$. In numerical simulations the problem is easily circumvented, as one can "tune" the simulated pulses for one specific point, in which the pulses are resonant and produce the desired 90° and 180° flip angles. In the following, RF pulses are sometimes referred as 90° and 180° pulses meaning that the tilt angle assumes these values for a well-defined voxel.

Experimental echo trains measured by the NMR-MOUSE are compared to simulated data for the Carr–Purcell XY16 sequence (*21, 22*) applied to a silicon rubber sample (*29*), (cf. Figs. 4a (simulation) and 4c (experimental)). Replacing the 180° refocusing pulses by 90° pulses greatly changes the pattern of the echo train (cf. Figs. 4b (simulation) and 4d (experimental)). In order to improve the agreement of simulated and experimental data an exponential transverse relaxation was introduced between the pulses, considering $T_1 \gg T_2$. Relaxation during the pulses was neglected. These particular
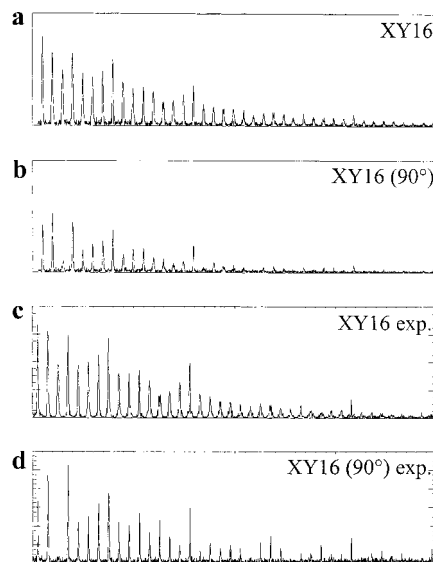
a

b

c

d

FIG. 4. Numeric simulation of echo trains for the Carr–Purcell-like pulse sequence with the XY16 phase cycle (*21, 22*) (a) and after replacing the 180° refocusing pulses by 90° pulses (b). A ^{1}H echo train recorded experimentally (*29*) corresponding to a XY16 (c) and XY16(90°) (d) pulse sequences.
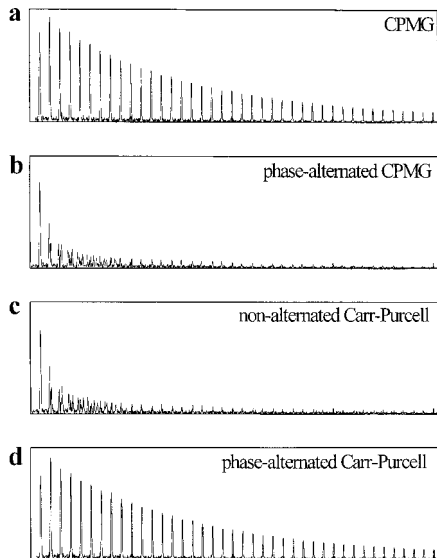
FIG. 5. Numerical simulation of echo trains for various Carr–Purcell-like pulse sequences. All signals are in the magnitude mode and echoes are artificially broadened. (a) CPMG: $\alpha_x-[\tau-\beta_y-\tau]_n$. (b) CPMG-type pulse sequence with alternated phases of the β pulses: $\alpha_x-[\tau-\beta_y-2\tau-\beta_{-y}-\tau]_n$. (c) Carr–Purcell pulse sequence without phase alternation: $\alpha_x-[\tau-\beta_x-\tau]_n$. (d) Carr–Purcell sequence with phase alternation: $\alpha_x-[\tau-\beta_x-2\tau-\beta_{-x}-\tau]_n$.

pulse sequences were chosen for comparison of simulation and experimental results because of the irregular trend of echoes they generate. The differences between the simulations (cf. Figs. 4a and 4b) and the experiments presented in Figs. 4c and 4d can be explained by small pulse misadjustments.

Carr–Purcell-like Pulse Sequences

In inhomogeneous fields, some pulse sequences, for instance, the phase-alternated Carr–Purcell ($\alpha_x-[\tau-\beta_x-2\tau-\beta_{-x}-\tau]_n$), (*18*) and Carr–Purcell–Meiboom–Gill (CPMG) ($\alpha_x-[\tau-\beta_y-\tau]_n$) (*19*), where α and β are the local flip angles around the effective fields, tend to produce more regular echo trains while others generate irregular echo trains, with distorted echoes, for instance, the Carr–Purcell-like sequences XY8 and XY16 (*21, 22*) and the phase-alternated CPMG sequence. Pulses of α type are those intended to be 90° pulses and in the simulations they are for the single voxel selected for their tuning, while β pulses are tuned to be 180° pulses at the same voxel. The numerical simulations of the echo trains presented in Figs. 5a and 5d show that the "good" sequences, CPMG and the phase-alternated Carr–Purcell sequences, generate similar echoes in the magnitude mode. These echoes decay with a decay time $T_{2\text{eff}}$, in this case roughly 1.5 times shorter than the value of T_2 used in the simulations. A change in the strength or length of the refocusing pulses will change this value as the pulses go away from the nominal 180° value. Actually, this property can be used to experimentally select nominal 180° pulses in inhomogeneous fields, defining them as the refocusing pulses in a CPMG or phase-alternated Carr–Purcell sequences that pro-

duce the fastest relaxation rate of the echo train for a sample with $T_2 \ll T_1$.

When no relaxation is included in these simulations, the good sequences will generate echoes that look almost identical after some oscillations (*30*) in the first few echoes. The echo's maximum amplitude is either the second or the third if refocusing pulses are not far from the 180° value, depending on the 90° pulse being half the strength or half the length of the 180° pulses.

Other Carr–Purcell-like pulse sequences produce shorter echo trains, with a nonexponential echo envelope. Such echo trains decrease in amplitude even if no transversal and longitudinal relaxation is included in the simulations. In order to understand this behavior, the first echoes generated by such pulse sequences were decomposed using numerical simulations by increasing the time interval between the pulses in the sequence in an irregular manner. Thus, instead of a pulse sequence P0$-\tau-$P1$-2\tau-$P2$-2\tau-$P3$-\tau$, the system response to a sequence P0$-\tau_1-$P1$-\tau_2-$P2$-\tau_3-$P3$-\tau$ was simulated with $\tau_1 = 0.1$ ms, $\tau_2 = 2.2\tau_1$, and $\tau_3 = 2.5\tau_1$. The RF pulses are denoted by Pn ($n = 0, 1, 2, 3$). The amplitude and phases of the pulses correspond to the values already discussed in the pulse sequences above. Numerically simulated signals s_y, s_x, and s_{magn} are presented in Fig. 6 for several Carr–Purcell-like pulse sequences. It is evident that the second echo generated for $\tau_1 = \tau_2$ decomposes into two elementary inhomogeneous echoes when $\tau_1 \neq \tau_2$ (known as *pathways* from Refs. (*26*), (*30*), and (*31*)), while the third decomposes into five *elementary echoes,* as opposed to four in Ref. (*26*) and in agreement with Ref. (*30*). Therefore, these simulations directly prove that the echoes generated by the Carr–Purcell-like pulse sequences are *mixed echoes.*

These simulations clearly show why some sequences are good, i.e., generate regular echo patterns, while others produce irregular echo trains. It is simply because the various echoes into which a mixed echo decomposes can all be of the same phase or not. It is interesting to note at this point that the echo E5 in Fig. 6a is an echo with positive amplitude, in phase with its neighbors. The widespread perception that in a Carr–Purcell sequence the alternation of the phases of the refocusing pulses cancels small errors in the pulse definition instead of adding them up fails to explain why in inhomogeneous fields a phase-alternated CPMG (i.e., $90°_x-[\tau-180°_y-2\tau-180°_{-y}-\tau]_n$) produces a train of distorted echoes while this is not the case for an in-phase CPMG sequence. The elementary echoes simulated in Figs. 6a to 6d graphically explain why the phases of the refocusing pulses should be the same in a CPMG sequence and why they should be alternated in a Carr–Purcell sequence.

The identification of the eight pure echoes into which the first three echoes of a standard Carr–Purcell-like pulse sequence are decomposed is quite straightforward. All of them derive from the FID of pulse P0, henceforth denoted "0," but not represented in the picture because it is not experimentally available. In order not to obtain an FID smaller than the
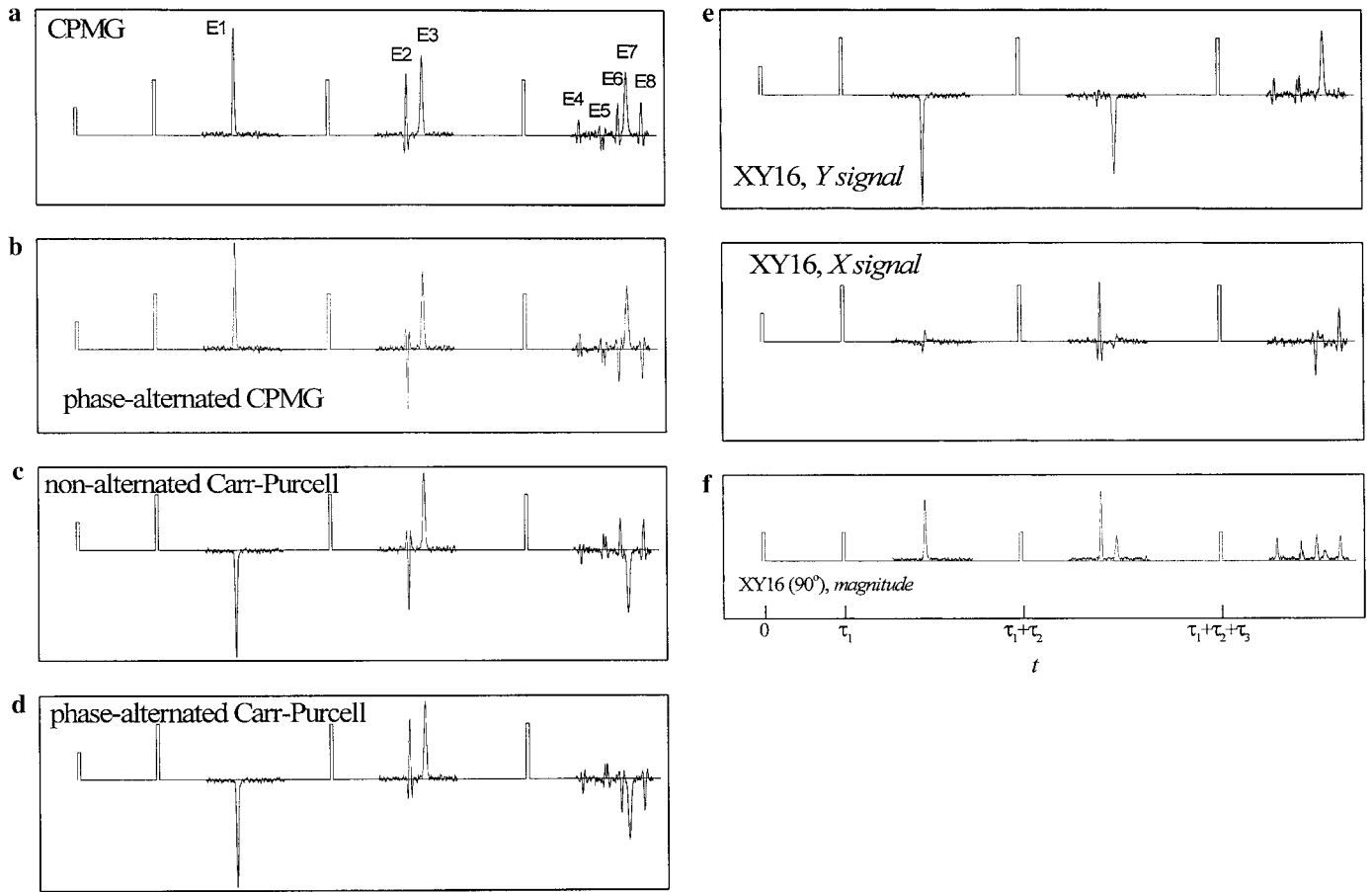
FIG. 6. Numerical simulation showing the decomposition of the first three echoes for several pulse sequences, obtained by increasing the distance between the RF pulses from that in the original sequences (see text). The Hahn and stimulated echoes for CPMG (a), phase-alternated CPMG (b), standard Carr–Purcell (c), phase-alternated Carr–Purcell (d), XY16 with detected *y*-signals (e1), XY16 with detected *x*-signals (e2), and XY16 with 90° pulses (f) are presented. All echoes are *y*-phase signals if not otherwise indicated. The time axis is the same for all simulations and is indicated in (f).

subsequent echoes, in the numerical simulations one has to extrapolate the FID from the end of the pulse backward to its middle. All elementary echoes are either Hahn echoes (denoted by H_i which means: "the Hahn echo generated by the RF pulse Pi") or stimulated echoes (denoted by S_{ij}, with $j > i$, (i, j) being the two RF pulses involved). Thus all of the echoes can be identified and traced back to the original FID, as E1 = $H_1(0)$, E2 = $S_{12}(0)$, E3 = $H_2(E1) = H_2(H_1(0))$, and so on (see Table 1 and Fig. 6a). These notations are just a stenographic way of keeping track of the echoes and one should keep in mind that E5 = $S_{13}(0)$, for instance, is not a pure product of P0, P1, and P3 pulses but it is also affected by the P2 pulse. Also E4 = $H_2(0)$ is also affected by the P1 and P3 pulses, not only by its "refocusing" pulse P2. In the absence of the P2 pulse, the echo E5 would look like the echo E3 (cf. Fig 6a), while, where the P1 and P3 pulses are eliminated, the echo E4 would look like E1.

One should note the decay pattern of the ordinary Hahn echoes, that is of the echoes one expects in weakly inhomogeneous $\mathbf{B}_0$ fields for a $90°–\tau_1–180°–\tau_2–180°–\tau_3–180°–\tau$, stan-

dard Carr–Purcell pulse sequence. Even when no relaxation is included in the simulations, the echoes E1, E3, and E7 continuously decrease in amplitude. They are also narrower in frequency spread, as one can infer from their increased width in the time domain. This effect is reminiscent of a filter acting on

TABLE 1
The Nine Real Echoes (E4 to E12) Generated after the Last Pulse of the Three-Pulse Sequence P0–τ_1–P1–τ_2–P2–τ_3–P3

Nature of echo	Echo time τ after P3	Position on the time axis
E4 = $H_2(0)$	$\tau = \tau_1 + \tau_2 - \tau_3$	$t = 2\tau_1 + 2\tau_2$
E5 = $S_{13}(0)$	$\tau = \tau_1$	$t = 2\tau_1 + \tau_2 + \tau_3$
E6 = $S_{23}(H_1(0))$	$\tau = -\tau_1 + \tau_2$	$t = 2\tau_2 + \tau_3$
E7 = $H_3(H_2(H_1(0)))$	$\tau = \tau_1 - \tau_2 + \tau_3$	$t = 2\tau_1 + 2\tau_3$
E8 = $H_3(S_{12}(0))$	$\tau = -\tau_1 + \tau_3$	$t = \tau_2 + 2\tau_3$
E9 = $S_{23}(0)$	$\tau = \tau_1 + \tau_2$	$t = 2\tau_1 + 2\tau_2 + \tau_3$
E10 = $H_3(\underline{S}_{12}(0))$	$\tau = \tau_1 + \tau_3$	$t = 2\tau_1 + \tau_2 + 2\tau_3$
E11 = $H_3(H_1(0))$	$\tau = -\tau_1 + \tau_2 + \tau_3$	$t = 2\tau_2 + 2\tau_3$
E12 = $H_3(0)$	$\tau = \tau_1 + \tau_2 + \tau_3$	$t = 2\tau_1 + 2\tau_2 + 2\tau_3$

the signal which the pulses are supposed to refocus. These ordinary Hahn echoes are also the largest ones, as long as one deals with a sequence designed to generate just them. As one can see in Fig. 6f, this is by no means a general rule, the echoes in an uninterrupted Hahn series can be just a byproduct if the refocusing pulses are far from 180°. The echo E5 (cf. Fig. 6a) is typical for the pitfalls one can encounter when calculating the signal intensity only for the exact time of the echo peak, since in such calculations an echo like E5 could be easily overlooked, having the midtime amplitude close to zero.

The "numerical noise" present in the baseline of the simulated signal (cf. Fig. 6) is due to the finite number of the voxels used for static and radiofrequency fields computations. This noise is related to the finite accuracy of the numerical simulations leading to slightly different baseline signals between neighboring voxels. The simulations show that smaller numbers of voxels decrease the signal-to-noise ratio as the number of voxels increases the noise disappears. One should also take into account that only voxels where the condition $B_0 \cong \omega/\gamma$ is fulfilled contribute to the formation of the echoes, thus the number of voxels involved in the formation of an echo is smaller than the total number of voxels.

The Timing and Nature of Elementary Echoes

The exact times τ at which echoes of the FID generated by a pulse P0 occur after the last pulse of a sequence: P0–τ_1–P1–τ_2–P2–...–τ_N–PN–τ can be obtained by using a heuristic generating function

$$\exp(i\omega\tau_1) \times [\exp(i\omega\tau_2) + 1 + \exp(-i\omega\tau_2)] \ldots$$
$$\times [\exp(i\omega\tau_N) + 1 + \exp(-i\omega\tau_N)]$$
$$\times [\exp(i\omega\tau) + \exp(-i\omega\tau)]. \qquad [17]$$

This function can be decomposed in $2 \times 3^{N-1}$ terms. An echo will occur every time one of the terms in Eq. [17] equals 1. A more complete formula would contain an amplitude factor for each term in Eq. [17] and could also predict the amplitude of each echo. If the pulse sequence is of the Carr–Purcell type, i.e., $\tau_2 = \tau_3 = \ldots = \tau_N = 2\tau_1$ and $\tau_1 = \tau$, one can substitute $\exp(i\omega\tau)$ by x and get a modified form of the generating function (*30*),

$$x \cdot \left(x + \frac{1}{x}\right) \cdot \left(x + 1 + \frac{1}{x}\right)^{N-1}, \qquad [18]$$

where the value of the x-independent term in Eq. [18] is the number of pathways or elementary echoes that build the Nth echo. In our particular case, P0–τ_1–P1–τ_2–P2–τ_3–P3–τ–echo, there are 18 terms that will yield for τ, 9 positive and 9 negative values. The positive values correspond to the echoes listed in Table 1, with their respective delays after
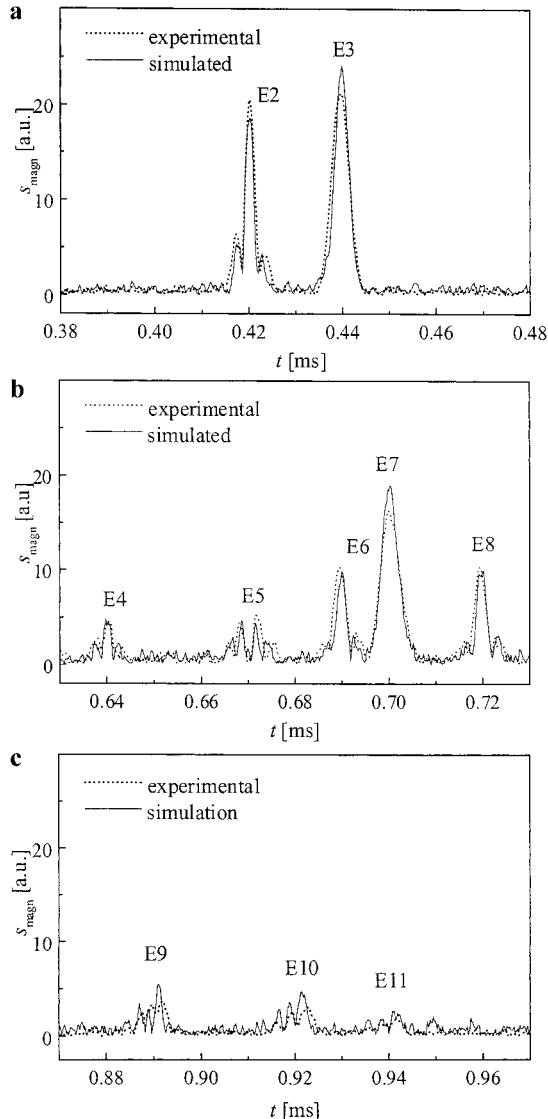

FIG. 7. Details of the decomposed echoes of the CPMG-like pulse sequences shown in Fig.6. Simulated and the experimental detected spin echoes on a silicon rubber sample are shown in magnitude mode. (a) Echoes E2 and E3. (b) Five echoes contributing to the third CPMG echo. (c) Three echoes that would add up to the fourth CPMG echo.

the pulse P3 and their positions t on the time axis measured from the first preparation pulse P0. All 9 echoes can readily be understood with the exception of echo E10 (see below). The elementary echoes E4–E8 are the 5 pathways that lead to the third mixed echo of a normal, Carr–Purcell-like sequence, E9–E11 represent 3 of the 13 pathways to a fourth mixed echo of the same sequence, and E12 should contribute to the fifth mixed echo. Figure 7 shows a comparison of calculated and measured elementary echoes for the groups E2–E3, E4–E8, and E9–E11. The simulated echoes are just the magnitude mode of the echoes shown in Fig. 6a, calculated as

$$s_{\text{magn}}(t) = \sqrt{s_x^2(t) + s_y^2(t)}. \qquad [19]$$

The experimental proton echoes presented in Fig. 7 were recorded on a silicone rubber sample using the NMR-MOUSE probe (12–16) driven by a Bruker Minispec whose characteristics were employed in the calculations of $\mathbf{B}_0$ and $\mathbf{b}_{1n}$. The amplitude of the simulated echo was scaled to the experimental one by a factor that was the same for Figs. 7a, 7b, and 7c. The agreement between the simulations and experiments is good, and the observable differences between the larger simulated regular successive Hahn echoes E3 and E7 and the smaller experimental ones can be attributed to deficiencies in the adjustment of the nominal 180° pulses in the experiment. This suggests that the refocusing 180° pulses be employed for tuning the flip angle, i.e., for trying to maximize the elementary echo $H_N(H_{N-1}(\ldots H_1(0) \ldots))$ compared to the other "irregular" echoes in the decomposition of the Nth Carr–Purcell or CPMG mixed echo.

Virtual Echoes

The nine negative solutions that should be added to Table 1 are not real echoes, but they should be nevertheless considered, because any one can be refocused later into real Hahn or real stimulated echoes by the subsequent pulses P4, P5, etc., which follow the pulse P3. Instead of discussing all nine of them a shorter sequence, $P0-\tau_1-P1-2.2\tau_1-P2-\tau$, is considered. Using the generating function of Eq. [17], one obtains three elementary echoes at positive times τ after the last pulse. They are E2, E3, and another echo that coincides with E4 in Fig. 6a but looks different as a result of the absence of pulse P3. One also obtains three negative solutions for τ, that is the entities V0 at $\tau = -\tau_1 - \tau_2$ corresponding to an echo at position $t = 0$, V1 at $\tau = \tau_1 - \tau_2$ for $t = 2\tau_1$, and V2 at $\tau = -\tau_1$ for $t = \tau_2$. The first corresponds to the FID after the pulse P0. The second solution constitutes the echo E1 or, better, what remains of it after the pulse P2, because the next pulse P3 refocuses V0 and V1, not FID(P0) and E1. The third entity, V2, corresponds to no observable echo. It corresponds to a *virtual echo,* or a *virtual stimulated echo* of the FID following the pulse P0. This virtual echo at $t = \tau_2$, that is at a negative $\tau = -\tau_1$ *before* the final pulse P2. It was denoted as V2 $= \underline{S}_{12}(0)$ in Table 1. The echo E10 cannot be understood without V2, as it cannot traced back to the FID(P0) through an uninterrupted chain of real Hahn and stimulated echoes. The echo E10 is the Hahn echo through P3 of this *virtual echo* $\underline{S}_{12}(0)$. It is called a *virtual echo* because it cannot be observed where it should be at $t = \tau_2$, but can be *seen* and refocused by the later pulse P3 into the real echo E10.

The fact that virtual echoes cannot be observed does not mean they cannot be simulated. In order to simulate the virtual echoes V0 $= \underline{H}_2(\underline{H}_1(0))$, V1 $= \underline{H}_2(H_1(0))$, and V2 $= \underline{S}_{12}(0)$, one has to simulate the evolution of the spin system until *after* the pulse P2 (or the last pulse of a sequence) and then evaluate
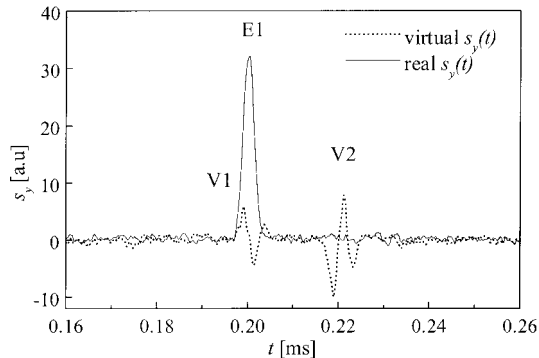

FIG. 8. Numerically simulated signals between the first refocusing pulse and the second one in the stretched CPMG pulse sequence (full line), and virtual echoes calculated using the following steps: RF pulse P0, free evolution during τ_1, RF pulse P1, free evolution during τ_2, RF pulse P2, free evolution computed backward, with a negative time increment (dotted line).

the system evolution *backward,* disregarding pulses, to $t = 0$. This "signal" calculated backward into the past displays all of the virtual echoes. These virtual echoes can be characterized by amplitudes, shapes in the time domain, and distributions in space and frequency. But similar to virtual images in optics, which cannot be projected onto a screen, they do not induce a signal in the NMR probe until another RF pulse corresponding to another lens is employed to refocus them. Figure 8 compares the simulated virtual echoes V1 and V2 to the real signal along the positive time axis. The difference between real echo E1 $= H_1(0)$ and virtual echo V1 $= \underline{H}_2(H_1(0))$ is striking. The virtual echo V1 is actually what remains of the elementary echo E1 after the pulse P2 for the subsequent pulse P3 to refocus, because what the subsequent pulse "see" is V1 and not E1. The virtual Hahn echo V1 is the virtual pair of the real echo E3, and the virtual stimulated echo V2 is the virtual pair of the real echo E2. Moreover, the echo E11 should be written as $H_3(V1) = H_3(\underline{H}_2(H_1(0)))$ instead of $H_3(E1) = H_3(H_1(0))$.

To summarize all of these results, one can say that in inhomogeneous fields: (i) Any pulse that comes at $t + \tau$ after a signal (FID or echo) at time t produces a real Hahn echo at time $t + 2\tau$ and a virtual echo at time t that constitutes a portion of the signal which remains from the original signal for the subsequent pulses. (ii) Any RF pulse inserted at time $t - \tau$ before an echo (that is produced otherwise by some previous pulses) at time t will generate a real echo at time t that is the echo modified by the new pulse and a virtual echo at time $t - 2\tau$. By this rule, the echo E4 should be written as $H_3(H_2(\underline{H}_1(0)))$, which is quite confusing, but nevertheless useful because this notation specifies that while the position of E4 depends on the position of P2 the amplitude and shape of E4 depend also on P1 and P3. (iii) Any pair of pulses i and j, $j > i$, at times $t + \tau_1$ and $t + \tau_1 + \tau_2$ positioned after a signal at time t will generate, in addition to the Hahn echoes, a real stimulated echo at time $t + 2\tau_1 + \tau_2$ and a virtual stimulated echo at time $t + \tau_2$. One should keep in mind that a stimulated
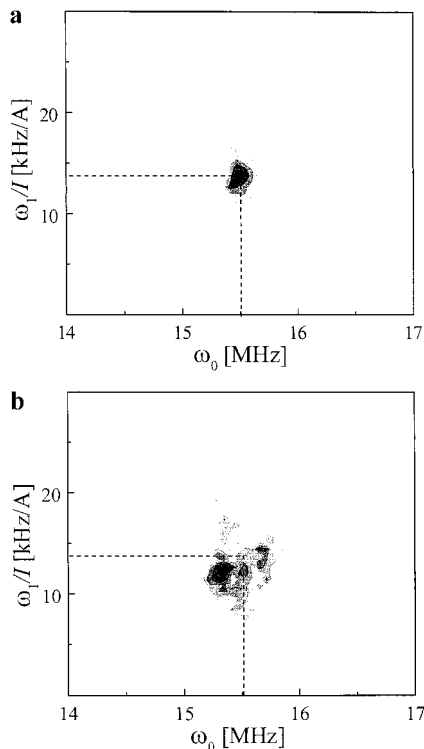
FIG. 9. Two-dimensional distributions of amplitude versus $\omega_0 = \gamma B_0$ and $\omega_1/I = \gamma b_{1n}$ for the stimulated echo E2 (b) and secondary Hahn echo E3 (a). These echoes are components of the second CPMG echo (cf. Fig. 6a). The (ω_0, ω_1/I) coordinates corresponding to the points $\mathbf{r} = (0, 0, 0)$, for which the sequence was tuned, are indicated by the dashed lines.

echo generated by pulses i and j will be shaped and modified by all intermediary pulses $i + 1$, $i + 2$, ..., $j - 1$. (iv) Any pair of pulses with the first pulse at $t - \tau_1$ before a signal which is otherwise produced by previous pulses at time t, and the second pulse at time $t - \tau_1 + \tau_2$, will generate a real stimulated echo at time $t + \tau_2$ and a virtual stimulated echo at $t - 2\tau_1 + \tau_2$ in addition to the Hahn echoes. Virtual echoes are a useful tool in understanding the formation of echoes in inhomogeneous fields, because they help explain every inhomogeneous echo generated by an arbitrary pulse sequence in terms of successive Hahn and stimulated echoes, either real or virtual.

Frequency Distributions of Echoes

Each of the echoes discussed above and presented in Figs. 5 to 8 has its own characteristics. The variations in the individual shapes and amplitudes of echoes in the time domain correspond to different frequency and b_{1n} distributions of the signals. In Fig. 9 two-dimensional distributions of the echoes E3 and E2 (see Fig. 6a) are plotted as a function of ω_0 and ω_1/I. It is easy to see that, as the CPMG sequence with the increasing echo time (cf. Fig. 6a) is designed to generate Hahn echoes, the Hahn echo E3 is the one that appears, as a sharp peak, at the

position for which the sequence was designed in the simulations. The "parasite" echo E2 arises from the inhomogeneities of $\mathbf{B}_0$ and $\mathbf{b}_{1n}$, and it derives from nearby regions, both in the $\mathbf{B}_0$–$\mathbf{b}_{1n}$ plane and in the three-dimensional volume occupied by the sample.

THE SENSITIVE VOLUME OF THE NMR-MOUSE

Due to the inhomogeneity of the fields a limited distribution of NMR signal in $\mathbf{B}_0$ and $\mathbf{b}_{1n}$ means a limited distribution of the signal in the sample volume. This fact is also applicable to the two echoes E2 and E3 discussed above.

Spatial Distribution of Echoes

In order to show the difference between the space distribution of the two echoes, the signal density S_y, as defined in Eq. [14], is plotted in Fig. 10 for a vertical slice, across the gap, through the center of the RF coil (the $x = 0$ plane). The stimulated echo (Fig. 10b) seems to surround the Hahn echo (Fig. 10a). The scale of the figures also provides information about the resolution of the NMR-MOUSE when applied to the surface of the sample. The two echoes, when superposed (that is for $\tau_2 = 2\tau_1$ in the terms of Fig. 5) together, form the second echo of the CPMG sequence, which is often the largest one.

It has been shown (*15, 16*) that a change in the transmitter frequency of the NMR-MOUSE produces a change in the sensitive volume of the device, more specifically in the depth of the slice that is producing the NMR signal. Because each echo is different, one can very well assume that the sensitive volume varies with each echo in a train of echoes generated by the sequence. In Fig. 11 projections of the signal density S_y
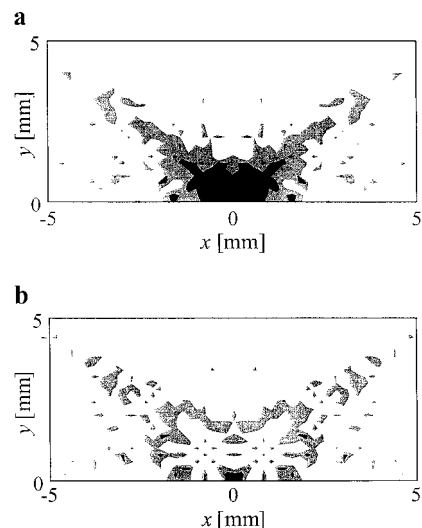

FIG. 10. The spatial distribution (sensitive volume) of the amplitude for the stimulated echo E2 (b) and Hahn echo E3 (a) which are components of the second mixed CPMG echo. A numerical filter with a bandwidth 300 kHz was applied.
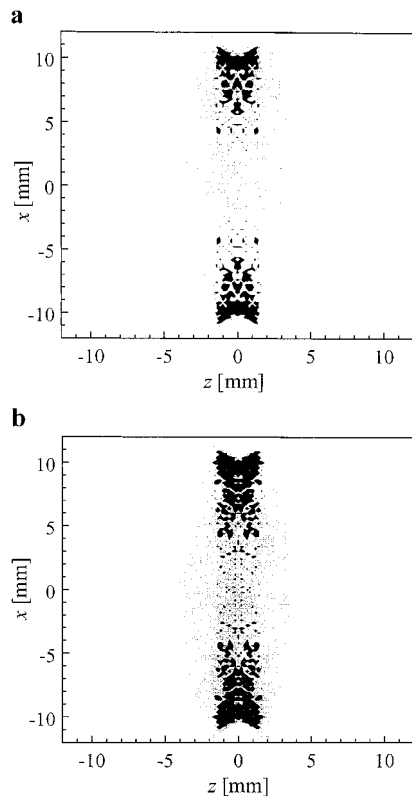
a

b

FIG. 11. Horizontal projection of the signal density for the first (a) and the ninth (b) echo of a CPMG sequence tuned for a point $\mathbf{r} = (0, 3\ \text{mm}, 0)$. The gray shading is proportional to the value of $\int_0^\infty S(x, y, z) dy$. A numerical filter with a bandwidth of 300 kHz was applied.

onto the z–x plane are depicted. This plane forms the surface of NMR-MOUSE. The projections are shown for the first Hahn echo (cf. Fig. 11a) and the ninth mixed echo (cf. Fig. 11b) of a CPMG echo train. The pulse sequence was tuned to a point 3 mm away from the surface of the NMR-MOUSE on the symmetry axis of the RF coil. A frequency filter with a rectangular bandwidth of 300 kHz was applied in the numerical simulations.

The first echo is a primary Hahn echo, while the ninth echo is composed of a multitude of elementary echoes. One can see that the change in the sensitive volume is not dramatic because the stimulated echoes and other "irregular" echoes tend to collect signals from space excluded from the "regular" echoes $H_n(\dots H_2(H_1(0)) \dots)$, that dwindles both in the frequency domain and in the spatial domain with increasing n. There is a certain increase in the overall intensity (corresponding to a slightly thicker slice) and a small lateral growth of the selected slice. This is due to the fact that relaxation was not included in these numerical simulations and thus the first echo is the smallest of the train. Geometrically, Figs. 11a and 11b, which represent the sensitive volumes, are slices that closely follow the saddle-shape surface of $\mathbf{B}_0(\mathbf{r})$ in Fig. 1b. They cross the saddle point and extend a little upward with increasing x and y.

Both ends of the darker strip seen in projections in Fig. 11 are signals from voxels near the NMR-MOUSE.

The thickness of the selected slices can best be evaluated from the frequency spectrum of the echoes. Figure 12 shows the frequency spectrum of the two echoes discussed above, before frequency filtering. The ninth mixed echo is slightly wider in frequency and more intense. The amplitude of this echo is given by the integral area of the frequency distribution. The larger spectral amplitude of the ninth mixed echo actually corresponds to a larger width of the selected slice.

The Shape of the Selected Volume

In order to visualize the sensitive volume of the NMR-MOUSE for a pulse experiment the signal density for the second, and largest, echo of a CPMG sequence was calculated for a nominal depth of 5 mm inside the sample volume. Figure 13 shows a vertical slice which contains the y axis through the sample volume at $z = 0$ along the gap of the permanent magnets (a) and a slice at $x = 0$, across the gap (b). A simulated projection of the sensitive volume onto the surface of the NMR-MOUSE given by signal density integrated along y axis is shown in Fig. 13c. The sensitive volume looks like an elliptical patch which extends along the saddle-shape resonant surface of Fig. 1a. The slice is thicker in the middle and thinner toward the edges. When the intensity of the RF pulses is increased and their length accordingly shortened the bandwidth of the echoes increases and the excited slice becomes thicker and somewhat larger. Figures 13d, 13e, and 13f show the two vertical slices and a horizontal projection of the signal density for the same sequence but with the power of the RF pulses increased. One can see that the sensitive volume becomes thicker without a significant increase in the lateral extension of the signal.

The discontinuities in the representation of the sensitive volume in Fig. 13 are artifacts that appear because of the relatively small number of voxels involved in simulating the
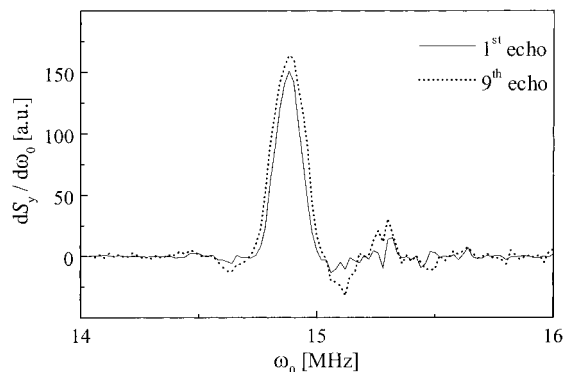

FIG. 12. Frequency distribution of the amplitude of the first echo, a Hahn echo, and the ninth echo, a mixed echo of a CPMG sequence tuned for the point $\mathbf{r} = (0, 3\ \text{mm}, 0)$. The ninth echo is broader in the frequency domain (thicker selected slice) and higher in spectral intensity (larger slice width).
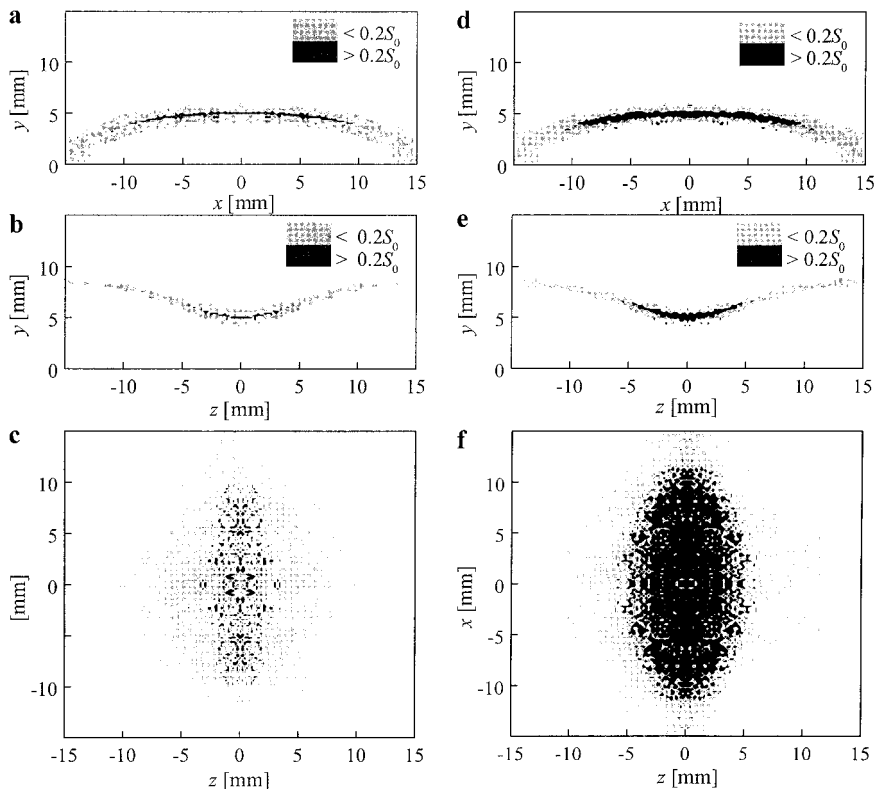
FIG. 13. The sensitive volume for the second, mixed echo of a CPMG pulse sequence, at a nominal depth of 5 mm inside the sample. (a) Signal density in a vertical slice along the gap at $z = 0$. (b) Vertical slice across the gap, at $x = 0$. (c) Projection of the signal density onto the surface of the NMR-MOUSE at $y = 0$. (d), (e), and (f) are the same as (a), (b), and (c) but with RF pulse intensity increased threefold and the pulse length accordingly shortened. S_0 denotes $S_{max}(0, 0, 0)$.

echo. Less than 1% of the total number of voxels contribute to the NMR signal in Figs. 13a to 13c and less than 2% to the enhanced signal in Figs. 13d to 13f.

The Depth Selectivity of the NMR-MOUSE

An experimental determination of the sensitive volume for a particular frequency of the transmitter and a particular pulse sequence is quite difficult, because it requires moving a minute sample from voxel to voxel. Hence a poor signal-to-noise ratio and long recording times are needed. Nevertheless, an experimental confirmation can be obtained from integrated NMR signals having the depth as a variable.

The depth of the selected slice can be changed by changing the transmitter frequency. The depth distribution of the signal has been computed according to

$$\frac{\partial S_y}{\partial y} = \int_x \int_z S_y(\mathbf{r}) dx dz, \qquad [20]$$

where $S_y(\mathbf{r})$ is the signal density at the time of a particular echo. By tuning the RF pulses for different depths y one can obtain different depth distributions. Figure 14 shows the sim-

ulated depth distributions for sequences tuned at $\mathbf{r} = (0, 1.6$ mm, $0)$ and $\mathbf{r} = (0, 2.8$ mm, $0)$ against the experimental results obtained with two different transmitter frequencies for an NMR-MOUSE. Both for the simulated and for the experimental data the signal employed was a Hahn echo generated by the sequence $90^{\circ}_x{-}\tau{-}180^{\circ}_y$. There is good agreement between simulated and measured data.
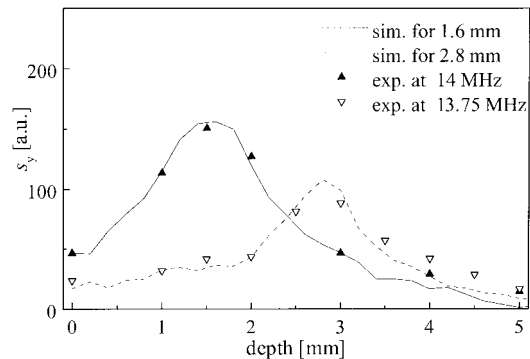

FIG. 14. Depth dependence of the signal intensity S_y for simulated Hahn echoes with pulse sequences tuned to nominal depth of 1.6 and 2.8 mm and for experimental measurements at 14 and 13.75 MHz on silicon rubber slices of 1-mm thickness.

CONCLUSIONS

A numerical simulation procedure has been developed for evaluation of the spin system response for an ensemble of isolated spins $\frac{1}{2}$ in inhomogeneous static and RF fields. This procedure was applied for the magnetic-field configuration of a NMR-MOUSE and can be extended to other configurations. In the simulation of the spin response the effects of the RF pulse can be separated from the effects generated by spin relaxation.

Carr–Purcell-like pulse sequences (18–22) represent an important NMR technique for obtaining relaxation information and have been applied in connection with the NMR-MOUSE (12–16). Therefore understanding the spin response for such a pulse sequence is of importance. The numerical simulations of the echo train for various Carr–Purcell-like pulse sequences show that intensity, shape, and phase of the echoes change along the train even in the absence of the relaxation effects. A truncated Carr–Purcell-like pulse sequence with three refocusing pulses with different pulse intervals was used to demonstrate the existence of mixed echoes. These echoes are a superposition of real Hahn and stimulated echoes of the original FID or of real and virtual preceding echoes. The echoes originate in different volumes of the sample with different static and RF fields, and their superposition leads to various intensities, shapes, and phases of mixed echoes in the echo train. Based on these results it was proven that in the absence of spin relaxation Carr–Purcell–Meiboom–Gill (19) and Carr–Purcell (18) pulse sequences generate echoes that look almost identical after some oscillations in the first few echoes. An important implication of these results is that in the presence of transversal and longitudinal relaxation these pulse sequences generate an almost exponential decay of the echo train, with a decay time different from both T_2 and T_1.

Sensitive volumes for different echoes along the echo train of Carr–Purcell-like pulse sequences can be simulated by the numerical procedure developed and their dependence on the pulse sequence parameters has been investigated.

Using the numerical simulation of the spin response for an NMR experiment performed in inhomogeneous fields, a better understanding of the experiments performed with the NMR-MOUSE can be achieved. The effects of longitudinal and transversal relaxation as well as self-diffusion can be included in the simulation procedure. Moreover, the effect of the dipolar couplings can be also taken into account. Work along these lines is in progress.

ACKNOWLEDGMENTS

REFERENCES

1. R. R. Ernst, G. Bodenhausen, and A. Wokaun, "Principles of Nuclear Magnetic Resonance in One and Two Dimensions," Oxford Univ. Press, Oxford (1987).

2. C. Slichter, "Principles of Magnetic Resonance," 3rd ed. Springer, Berlin (1990).

3. K. Schmidt-Rohr and H. W. Spiess, "Multidimensional Solid State NMR and Polymers," Academic Press, New York (1994).

4. R. Kimmich, "NMR, Tomography, Diffusiometry, Relaxometry," Springer, Berlin (1997).

5. D. Canet, "Nuclear Magnetic Resonance: Concepts and Methods," Wiley, Chichester (1996).

6. D. Canet, *Prog. NMR Spectrosc.* **30,** 101 (1997).

7. S. Berger, *Prog. NMR Spectrosc.* **30,** 137 (1997).

8. T. Fritzhanns, S. Hafner, D. E. Demco, H. W. Spiess, and F. H. Laukien, *J. Magn. Reson.* **134,** 355 (1998).

9. P. T. Callaghan, "Principles of Nuclear Magnetic Resonance Microscopy," Clarendon Press, Oxford (1991).

10. B. Blümich and W. Kuhn, (Eds.), "Magnetic Resonance Microscopy," VCH, Weinheim (1992).

11. P. Blümler, B. Blümich, R. Botto, and E. Fukushima, (Eds.), "Spatially Resolved Magnetic Resonance," Wiley–VCH, Weinheim (1998).

12. G. Eidmann, R. Salvesberg, P. Blümler, and B. Blümich, *J. Magn. Reson. A* **122,** 104 (1996).

13. G. Zimmer, A. Guthausen, U. Schmitz, K. Saito, and B. Blümich, *Adv. Mater.* **9,** 987 (1997).

14. B. Blümich, P. Blümbler, G. Eidman, A. Guthausen, R. Haken, U. Schmitz, K. Saito, and G. Zimmer, *Magn. Reson. Imag.* **16,** 479 (1998).

15. A. Guthausen, G. Zimmer, P. Blümler, and B. Blümich, *J. Magn. Reson.* **130,** 1 (1998).

16. G. Zimmer, A. Guthhausen, and B. Blümich, *Solid State Nucl. Magn. Reson.* **12,** 183 (1998).

17. G. A. Matzkanin, in "Nondestructive Characterization of Materials" (P. Höller, V. Hauck, C. O. Rund, and R. E. Green, Eds.), Springer-Verlag, Berlin (1989).

18. H. Y. Carr and E. M. Purcell, *Phys. Rev.* **94,** 630 (1954).

19. S. Meiboom and D. Gill, *Rev. Sci. Instrum.* **29,** 688 (1958).

20. A. J. Shaka, S. P. Rucker, and A. Pines, *J. Magn. Reson.* **77,** 606 (1988).

21. T. Guillon, D. B. Baker, and M. S. Conradi, *J. Magn. Reson.* **89,** 479 (1990).

22. T. Guillon, *J. Magn. Reson. A* **101,** 320 (1993).

23. D. E. Demco, A. Johansson, and J. Tegenfeldt, *J. Magn. Reson. A* **110,** 183 (1994).

24. M. McCaig, "Permanent Magnets in Theory and Practice," Pentech Press, London (1977).

25. J. D. Jackson, "Classical Electrodynamics," Wiley, New York (1975).

26. G. Goelman and M. G. Prammer, *J. Magn. Reson. A* **113,** 11 (1995).

27. J. R. Reitz and F. J. Milford, "Fundations of Electromagnetic Theory," Addison-Wesley, Reading (1967).

28. D. I. Hoult and E. R. Richarson, *J. Magn. Reson.* **24,** 71 (1976).

29. A. Guthausen, "Die NMR-MOUSE. Methoden und Anwendung zur Charakterisierung von Polymeren," dissertation, RWTH Aachen (1998).

30. A. D. Bain and E. W. Randall, *J. Magn. Reson. A* **123,** 49 (1996).

31. J. Hennig, *J. Magn. Reson.* **79,** 397 (1998).